

# Structure–Activity Relationship in Nanostructured Copper–Ceria-Based Preferential CO Oxidation Catalysts

D. Gamarra,<sup>†</sup> G. Munuera,<sup>‡</sup> A. B. Hungría,<sup>§</sup> M. Fernández-García,<sup>†</sup> J. C. Conesa,<sup>†</sup>  
P. A. Midgley,<sup>§</sup> X. Q. Wang,<sup>⊥</sup> J. C. Hanson,<sup>⊥</sup> J. A. Rodríguez,<sup>⊥</sup> and A. Martínez-Arias<sup>\*,†</sup>

*Instituto de Catálisis y Petroleoquímica, CSIC, C/Marie Curie 2, Campus Cantoblanco, 28049 Madrid, Spain, Departamento de Química Inorgánica e Instituto de Ciencia de Materiales, Centro Mixto Universidad de Sevilla-CSIC, 41092 Sevilla, Spain, Department of Materials Science, University of Cambridge, Cambridge CB23QZ, U.K., and Chemistry Department, Brookhaven National Laboratory, Upton, New York 11973*

*Received: March 21, 2007; In Final Form: May 21, 2007*

Two series of nanostructured oxidized copper–cerium catalysts with varying copper loadings, and prepared, respectively, by impregnation of ceria and by coprecipitation of the two components within reverse microemulsions, have been characterized in detail at structural and electronic levels by X-ray diffraction (XRD), Raman spectroscopy, high-resolution electron microscopy (HREM), X-ray energy dispersive spectroscopy (XEDS), X-ray photoelectron spectroscopy (XPS) (including Ar<sup>+</sup>-sputtering), and X-ray absorption fine structure (XAFS). These results have been correlated with analysis of their catalytic properties for preferential oxidation of CO in a H<sub>2</sub>-rich stream (CO-PROX), complemented by Operando–DRIFTS. A relevant difference between the two series of catalysts concerns the nature of the support for the surface-dispersed copper oxide entities, which is essentially ceria for the samples prepared by impregnation and a Ce–Cu mixed oxide for those prepared by microemulsion–coprecipitation. The existence of copper segregation in the form of copper oxide or copper-enriched Cu–Ce mixed oxides for the latter type of samples is uniquely revealed by nanoprobe XEDS and XPS Ar<sup>+</sup>-sputtering experiments. The CO oxidation activity under CO-PROX conditions is correlated to the degree of support-promoted reduction achieved by the dispersed copper oxide particles under reaction conditions. Nevertheless, catalysts which display higher CO oxidation activity are generally more efficient also for the undesired H<sub>2</sub> oxidation reaction. The balance between both reactions results in differences in the CO-PROX activity between the two series of catalysts which are examined on the basis of the structural differences found.

## 1. Introduction

Production of H<sub>2</sub> for polymer fuel cells (PEMFC) is usually accomplished by a multistep process that includes catalytic reforming of hydrocarbons or oxygenated hydrocarbons followed by water gas shift (WGS).<sup>1,2</sup> The gas stream obtained after these processes presents in most cases a relatively high CO concentration that disallows efficient handling of the fuel by the Pt alloy anode usually employed in the PEMFC. Preferential (or selective) oxidation of CO in the H<sub>2</sub>-rich stream resulting from such processes (CO-PROX) has been recognized as one of the most straightforward and cost-effective methods to achieve acceptable CO concentrations (below ca. 100 ppm).<sup>3–7</sup>

Different types of catalysts have shown their efficiency for the CO-PROX process. These can be classified into three general groups as a function of their nature and/or respective catalytic properties. The first group involves supported noble metal catalysts (mainly Pt ones) and follows from first developments done by Engelhard researchers in the context of processes related to ammonia production.<sup>8</sup> They present the main drawback of their relatively low selectivity for the process at practical

operating temperature (between 423 and 473 K), which can make necessary including interstage cooling operations to avoid extensive heating as a consequence of the exothermicity of the oxidation reactions involved.<sup>3,9</sup> A second group of active catalysts involves supported gold catalysts, well-known for their outstanding performance for CO oxidation.<sup>3,10–14</sup> These show a high CO-PROX activity with a good match between their activity window and the PEMFC anode operating temperature (353–403 K). However, they can present the drawback of their poor resistance to the presence of CO<sub>2</sub> in the reactant mixture.<sup>3,11,12,15</sup> The third group is constituted by catalysts based on closely interacting copper oxide and ceria, which have shown promising properties in terms of activity, selectivity, and resistance to CO<sub>2</sub> and H<sub>2</sub>O, while their lower cost could make them strongly competitive.<sup>3,4,6,7,16–22</sup>

The particular ability of the latter class of catalysts for the CO-PROX or related processes has been essentially attributed to the synergistic redox properties produced upon formation of copper oxide–ceria interfacial sites.<sup>4,6,17,18,23–28</sup> A previous work from our group was dedicated to analyze differences in the CO-PROX catalytic performances as a function of the support employed in a series of CuO/(Ce,M)O<sub>x</sub> (with M = Zr or Tb) catalysts.<sup>18</sup> In agreement with studies of a similar type,<sup>16,29,30</sup> it was shown that the CuO/CeO<sub>2</sub> configuration yielded best results in terms of both CO conversion and CO-PROX selectivity, which was generically attributed to the higher interfacial redox

\* Corresponding author. E-mail: amartinez@icp.csic.es.

<sup>†</sup> Instituto de Catálisis y Petroleoquímica, CSIC.

<sup>‡</sup> Centro Mixto Universidad de Sevilla-CSIC.

<sup>§</sup> University of Cambridge.

<sup>⊥</sup> Brookhaven National Laboratory.

activity of such catalyst.<sup>18</sup> In turn, selectivity differences between the catalysts were related to the structural/morphological properties of the copper oxide species present in each case.<sup>18</sup> Nevertheless, details are lacking with respect to the nature of the species or processes involved in the reaction mechanism and/or their respective evolutions during the catalytic process.<sup>6,17,23</sup> Generally speaking, the properties of copper entities for CO oxidation promotion apparently depend strongly on their dispersion degree and/or related degree of interaction with ceria.<sup>18,23,24,31</sup> Additionally, incorporation of copper into the fluorite network of ceria can induce important modifications on its chemical properties.<sup>32–35</sup>

Within this context, the present work aims to get further insights into the catalytic properties of catalysts based on combinations between copper and cerium oxides for CO-PROX. For this purpose, two series of catalysts differing in the preparation method employed have been characterized by different techniques (XRD, Raman, TEM–XEDS, XPS, and XAFS) and examined in parallel with respect to their catalytic performance for the CO-PROX process (complemented by Operando–DRIFTS spectroscopy analysis) in order to intend establishing structure–activity relationships for this type of system–process.

## 2. Experimental Section

**Materials.** Copper-doped ceria samples, labeled as  $\text{Ce}_{1-x}\text{Cu}_x\text{O}_2$  ( $x = 0.05, 0.1$ , and  $0.2$ ) were prepared with a modified reverse microemulsion method.<sup>34,36</sup> Briefly, the precursors (copper(II) and cerium(III) nitrates from Aldrich) were introduced in a reverse microemulsion (water in oil) using *n*-heptane as the organic phase, Triton X-100 (Aldrich) as surfactant, and hexanol as cosurfactant. Then, this suspension was mixed with another similar suspension containing as aqueous phase an alkali solution (TMAH, Aldrich) in order to coprecipitate the cations. The resulting mixtures were stirred for 24 h, centrifuged, decanted, and rinsed with methanol. Finally, the solid portion was dried overnight at 373 K, and the resulting powders were calcined under air at 773 K for 2 h. Inductively coupled plasma-atomic emission spectroscopy (ICP-AES) chemical analysis of these samples confirmed quantitative precipitation of both Cu and Ce cations.

Samples of copper supported on  $\text{CeO}_2$  (Cu wt % of 0.5, 1.0, and 5.0, denoted as 0.5CuO/ $\text{CeO}_2$ , 1CuO/ $\text{CeO}_2$ , and 5CuO/ $\text{CeO}_2$ , respectively; these correspond to Cu/Ce at. ratios of 0.011, 0.022, and 0.116, respectively) were prepared by incipient wetness impregnation of a  $\text{CeO}_2$  support prepared by microemulsion (in a similar manner as described above) with copper nitrate aqueous solutions. Following impregnation, the samples were dried overnight at 373 K and finally were calcined under air at 773 K for 2 h.

**Techniques.** Powder X-ray diffraction (XRD) patterns of the samples were recorded on a Seifert XRD 3000P diffractometer using nickel-filtered Cu K $\alpha$  radiation operating at 40 kV and 40 mA, using a 0.02° step size and 2 s counting time per point. Analysis of the diffraction peaks was done with the computer program ANALYZE Rayflex version 2.293.

Raman spectra were collected at room temperature using a Renishaw Dispersive System 1000 equipped with a cooled CCD detector and holographic Notch filter. The samples were excited with the red laser line (632.8 nm); the spectral resolution was 3  $\text{cm}^{-1}$ , and the spectrum acquisition consisted of two accumulations with a total of 10 min acquisition time.

High-resolution electron microscopy (HREM), high-angle annular dark field (HAADF) images, and X-ray energy disper-

sive spectra (XEDS) were recorded on a 200 kV FEI Tecnai F20-G2 scanning transmission electron microscope/scanning electron microscope (STEM/SEM) equipped with an EDAX r-TEM ultrathin window (UTW) X-ray detector. XEDS analysis was performed in STEM mode, with a probe size  $\sim 1$  nm. Specimens were prepared by depositing particles of the samples to be investigated onto a gold grid supporting a perforated carbon film. Deposition was achieved by dipping the grid directly into the powder of the samples to avoid contact with any solvent.

Cu K absorption edge XAFS spectra were collected in air at room temperature at beamline X18B of the NSLS at BNL. A commercially available Lytle cell was used for mounting the sample.<sup>37</sup> The X-ray absorption spectra were taken repeatedly in the “fluorescence-yield mode” using a pips (passivated–implanted planar silicon) detector cooled with circulating water. The monochromator was detuned 15% in order to reduce the amount of higher harmonics in the beam. The photon energy was calibrated for each scan with the first inflection point of the Cu K-edge in Cu metal foil. Both the incident ( $I_0$ ) and transmitted ( $I$ ) synchrotron beam intensities were measured simultaneously using an ionization chamber filled with 100%  $\text{N}_2$  gas and a mixture of 50% Ar and 50%  $\text{N}_2$ , respectively.

X-ray photoelectron spectra (XPS) were recorded with a Leybold–Heraeus spectrometer equipped with an EA-200 hemispherical electron multichannel analyzer (from Specs) and a 120 W, 30 mA Mg K $\alpha$  X-ray source. Ar<sup>+</sup>-etching treatments were carried out with a current of 6 mA and an acceleration voltage of 3.5 kV (ion current, 8  $\mu\text{A}$ ). This gave a sputtering yield rate of ca. 12  $\text{\AA}/\text{min}$ , according to a calibration made using a standard  $\text{Ta}_2\text{O}_5$  thin film electrochemically grown on a Ta foil. The samples (0.2 mg) were slightly pressed into a small ( $4 \times 4 \text{ mm}^2$ ) pellet and then mounted on the sample rod and introduced into the pretreatment chamber where they could be subjected to thermal or redox treatments under ca. 1 torr of reactive gases. Following each treatment, the sample was moved into the ion-pumped analysis chamber where it was further outgassed until a pressure less than  $2 \times 10^{-9}$  torr was attained (2–3 h). This low pressure was maintained during all the data acquisition by ion pumping of the chamber. After each treatment, XP spectra in the relevant energy windows were collected for 20–90 min, depending on the peak intensities, at a pass energy of 44 eV ( $1 \text{ eV} = 1.602 \times 10^{-19} \text{ J}$ ) which is typical of high-resolution conditions. The intensities were estimated by calculating the integral of each peak after subtraction of an S-shaped Shirley-type background with the help of UNIFIT for Windows (version 3.2) software;<sup>38</sup> atomic ratios were then derived using the appropriate experimental sensitivity factors. All binding energies (BE) were referenced to the adventitious C1s line at 284.6 eV. This reference gave BE values with an accuracy of  $\pm 0.1$  eV; the peak  $u'''$  characteristic of  $\text{Ce}^{4+}$  was thus obtained at  $917.0 \pm 0.1$  eV. In the case of Ce(3d) spectra, factor analysis (FA) was used to calculate the  $\text{Ce}^{3+}/\text{Ce}^{4+}$  ratios in each set of spectra recorded, using the methodology developed in a previous work.<sup>39</sup>

Operando–DRIFTS analysis was carried out using a Bruker Equinox 55 FTIR spectrometer fitted with an MCT detector. The DRIFTS cell (Harrick) was fitted with  $\text{CaF}_2$  windows and a heating cartridge that allowed samples to be heated to 773 K. Aliquots of ca. 100 mg were calcined in situ (in a similar way as employed for the catalytic tests, vide infra) and then cooled to 298 K under diluted oxygen before introducing the reaction mixture and heating in a stepped way, recording one spectrum (average of 50 scans at 4  $\text{cm}^{-1}$  resolution) typically every 10

**TABLE 1:**  $S_{\text{BET}}$  Values and Morphological/Structural Parameters Extracted from Analysis of the X-ray Diffractograms for the Copper–Ceria Samples and the Reference Ceria<sup>a</sup>

sample	$S_{\text{BET}}$ ( $\text{m}^2 \text{g}^{-1}$ )	lattice parameter (Å)	crystal size (nm)	microstrain ( $\Delta d/d$ )
CeO <sub>2</sub>	130	5.412	7.7	0.0019
0.5CuO/CeO <sub>2</sub>	116	5.410	7.6	0.0024
1CuO/CeO <sub>2</sub>	107	5.410	7.8	0.0025
5CuO/CeO <sub>2</sub>	101	5.413	8.1	0.0034
Ce <sub>0.95</sub> Cu <sub>0.05</sub> O <sub>2</sub>	130	5.410	7.0	0.0042
Ce <sub>0.9</sub> Cu <sub>0.1</sub> O <sub>2</sub>	136	5.413	6.8	0.0044
Ce <sub>0.8</sub> Cu <sub>0.2</sub> O <sub>2</sub>	151	5.413	6.6	0.0111

<sup>a</sup> Crystal size and microstrain values are based on analysis of the peaks by means of W–H linear fittings (ref 27).

K after the signal of different monitored gases (analyzed on line by means of a quadrupole mass spectrometer Pfeiffer Omnistar) becomes constant (i.e., steady conditions). The gas mixture (1% CO + 1.25% O<sub>2</sub> + 50% H<sub>2</sub> in He) was prepared using mass flow controllers with ca. 100 cm<sup>3</sup> min<sup>−1</sup> passing through the catalyst bed at atmospheric pressure, which corresponds to conditions similar to those employed for the reaction tests with the tubular reactor.

The catalysts calcined in situ (under oxygen diluted in Ar at 773 K) were tested in a glass tubular catalytic reactor for their activity under an atmospheric pressure flow (using mass flow controllers to prepare the reactant mixture) of 1% CO, 1.25% O<sub>2</sub>, and 50% H<sub>2</sub> (Ar balance), at a rate of  $1 \times 10^3 \text{ cm}^3 \text{ min}^{-1}$  (roughly corresponding to 80 000 h<sup>−1</sup> GHSV) and using a heating ramp of 5 K min<sup>−1</sup> up to 523 K. Analysis of the feed and outlet gas streams was done by gas infrared (Perkin-Elmer FTIR spectrometer model 1725X, coupled to a multiple reflection transmission cell—Infrared Analysis Inc. “long path gas minicell”, 2.4 m path length, ca. 130 cm<sup>3</sup> internal volume) while a paramagnetic analyzer (Servomex 540 A) was used to analyze the O<sub>2</sub> concentration. No products other than those resulting from CO or H<sub>2</sub> combustion (i.e., CO<sub>2</sub> and H<sub>2</sub>O; note that possible contributions of WGS or reverse WGS must be residual under the conditions employed and, if at all, would take place only at temperatures higher than ca. 473 K over these catalysts)<sup>40</sup> were detected in the course of the runs, in agreement with previous results on catalysts of this type.<sup>6,17,19,31</sup> On this basis, values of percentage conversion and selectivity in the CO-PROX process are defined as

$$X_{\text{O}_2} = \frac{F_{\text{O}_2}^{\text{in}} - F_{\text{O}_2}^{\text{out}}}{F_{\text{O}_2}^{\text{in}}} \times 100 \quad X_{\text{CO}} = \frac{F_{\text{CO}}^{\text{in}} - F_{\text{CO}}^{\text{out}}}{F_{\text{CO}}^{\text{in}}} \times 100$$

$$S_{\text{CO}_2} = \frac{X_{\text{CO}}}{2.5X_{\text{O}_2}} \times 100$$

where  $X$  and  $S$  are percentage conversion and selectivity, respectively, and  $F$  is the (inlet or outlet) molar flow of the indicated gas.

### 3. Results and Discussion

**Characterization.** Surface area values ( $S_{\text{BET}}$ ) for the samples prepared by microemulsion–coprecipitation (Ce<sub>1− $x$</sub> Cu <sub>$x$</sub> O<sub>2</sub>) are observed to increase with the copper content, in agreement with the gradual particle size decrease (Table 1). In contrast,  $S_{\text{BET}}$  values obtained for the samples prepared by impregnation are shown to decrease with the copper loading and in any case result lower than that of the parent CeO<sub>2</sub> support (Table 1), which

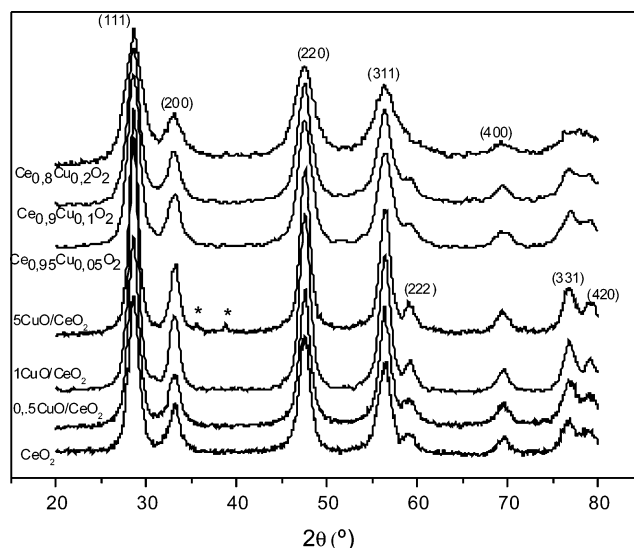


**Figure 1.** X-ray diffraction patterns of the indicated samples. Miller indexes for the fluorite diffractions are marked. Asterisk marks correspond to most intense peaks of tenorite CuO.

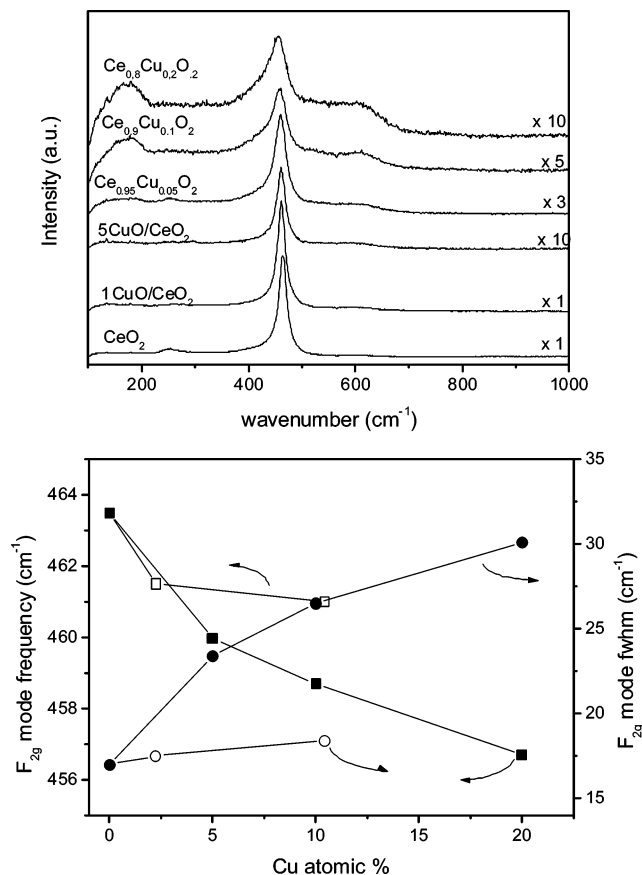


**Figure 2.** Top: Raman spectra of the indicated samples. Bottom: evolution of the frequency (squares) and width (circles) of the  $F_{2g}$  Raman band as a function of the copper content for the two series of samples: full symbols, Ce<sub>1− $x$</sub> Cu <sub>$x$</sub> O<sub>2</sub> samples; open symbols,  $x$ CuO/CeO<sub>2</sub> samples.

suggests a certain blocking of the pores of the support upon copper incorporation at its surface.

Figure 1 displays the X-ray diffractograms of the samples. Diffraction peaks attributable to the fluorite phase of ceria are observed in all cases. Analysis of the peaks by means of Williamson–Hall (W–H) plots (not shown) reveals that the particle size remains close to that of the parent CeO<sub>2</sub> sample



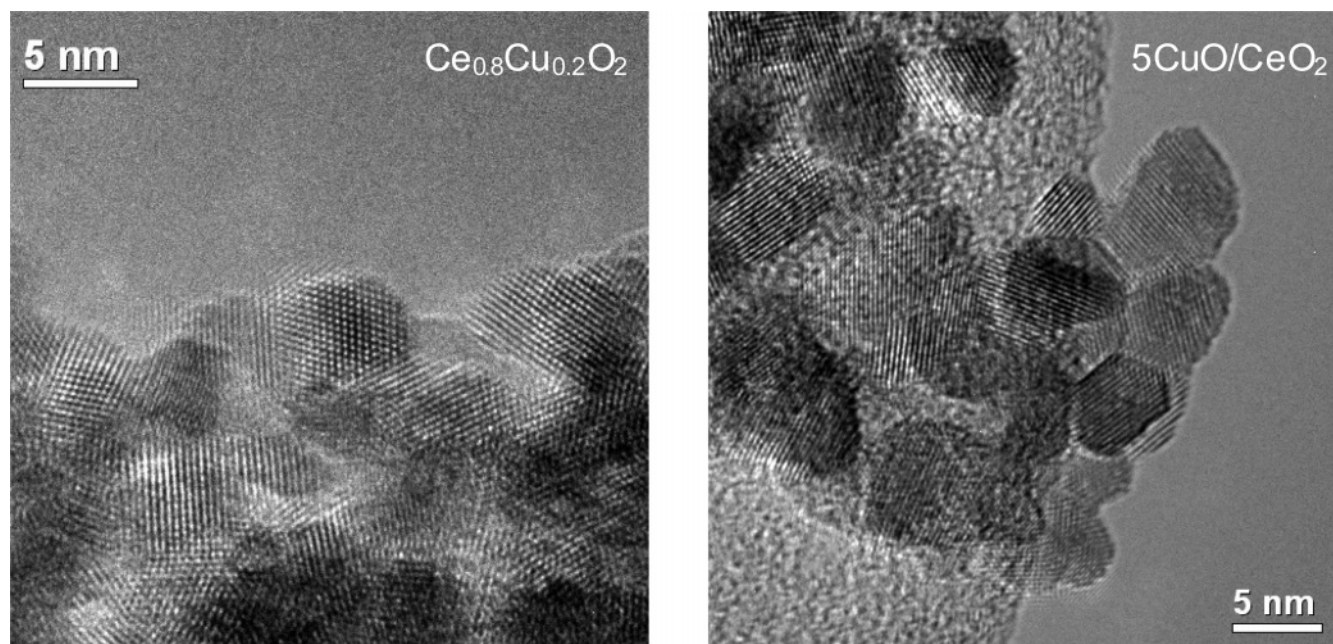


**Figure 3.** HREM pictures representative for the 5CuO/CeO<sub>2</sub> and Ce<sub>0.8</sub>Cu<sub>0.2</sub>O<sub>2</sub> samples.

for the samples prepared by impregnation, whereas it decreases with the copper content for the samples prepared by coprecipitation within reverse microemulsions, in good qualitative agreement with specific surface area values observed for the samples (Table 1). As collected in Table 1, lattice parameters estimated from peaks analysis are close to that expected for pure ceria for all the samples. However, it must be noted that this does not discard that Ce–Cu mixed oxide may have been formed in some case, as discussed in detail previously.<sup>34,41</sup> In this sense, microstrain values estimated from the W–H plots are only slightly higher to that of the parent CeO<sub>2</sub> for the samples prepared by impregnation, whereas they are appreciably higher and furthermore gradually increase with the copper content for the samples prepared by microemulsion (Ce<sub>1-x</sub>Cu<sub>x</sub>O<sub>2</sub> samples, Table 1). Such strong microstrain increase estimated for this type of sample must not be related to particle size effects which, if at all,<sup>42</sup> would produce much lower modifications in such parameter.<sup>43,44</sup> It rather suggests that copper has effectively been incorporated into the ceria fluorite lattice. Indeed, previous Rietveld refinement of synchrotron-derived X-ray diffraction data for the Ce<sub>1-x</sub>Cu<sub>x</sub>O<sub>2</sub> catalysts was consistent with substitutional Cu<sup>2+</sup> incorporation into the ceria lattice along with formation of oxygen vacancies for charge balance, in fair agreement also with density functional calculations.<sup>34</sup> As mentioned above, practically no change in cell dimension was estimated from those analyses when such substitutional copper incorporation occurs.<sup>34</sup>

The copper incorporation to the fluorite lattice in Ce<sub>1-x</sub>Cu<sub>x</sub>O<sub>2</sub> catalysts is also supported by Raman experiments, displayed in Figure 2. The spectra show a main band at about 460 cm<sup>-1</sup> which corresponds to the triply degenerate F<sub>2g</sub> mode of fluorite CeO<sub>2</sub> (the only one allowed in first order).<sup>45,46</sup> A general decrease of the intensity is observed with increasing the copper content in any of the series. This can be related to an increased optical absorption with increasing the copper content, on the basis of UV–vis results observed for samples of this kind,<sup>35</sup> although other physical phenomena related to lattice disorder cannot be discarded.<sup>47</sup> Nevertheless, comparison of the two series of catalysts reveals that while the presence of copper only slightly affects the spectrum of pure CeO<sub>2</sub> in the catalysts prepared by impregnation (which suggests only a small incor-

poration of copper at surface or subsurface positions of the lattice also for those samples,<sup>27</sup> in agreement with microstrain values observed for them, Table 1), it significantly affects the spectra of the Ce<sub>1-x</sub>Cu<sub>x</sub>O<sub>2</sub> series. First, a broad band extending between about 500 and 650 cm<sup>-1</sup>, which has been related to the presence of oxygen vacancies,<sup>48</sup> shows increasing relative intensity with increasing the amount of copper; it must be noted in this respect that the mentioned substitutional incorporation of Cu<sup>2+</sup> into the fluorite lattice must be accompanied by generation of oxygen vacancies (Ce<sup>4+</sup> + O<sup>2-</sup> ↔ Cu<sup>2+</sup> + V<sub>O</sub>; V<sub>O</sub> being a doubly ionized oxygen vacancy). Further evidence of copper incorporation in the lattice for the Ce<sub>1-x</sub>Cu<sub>x</sub>O<sub>2</sub> series is given by the shift and width observed in the main F<sub>2g</sub> mode band, as shown in Figure 2. These observables certainly present influences of both phonon confinement and oxygen vacancies, while inhomogeneous strain related to the presence of reduced states of cerium can be also involved.<sup>44,46,48</sup> In addition to the F<sub>2g</sub>-like contribution, a band centered at ca. 175 cm<sup>-1</sup> is detected which shows a relative growth with increasing copper content in the Ce<sub>1-x</sub>Cu<sub>x</sub>O<sub>2</sub> series, whereas the shape of the main band at ca. 460 cm<sup>-1</sup> suggests a concomitant relative growth of a new broad band centered at ca. 425 cm<sup>-1</sup>. This new band must not appear as an effect of phonon confinement, known to produce a low-frequency tail in the main band, since such strong asymmetry would not be expected in that case.<sup>46</sup> Rather the bands at 175 and 425 cm<sup>-1</sup>, which cannot be related to second-order bands,<sup>45,49</sup> can appear as a consequence of a copper-induced small tetragonal distortion (undetectable by XRD), compatible with previous theoretical calculations.<sup>34</sup> Additionally, the presence of a weak band at 294 cm<sup>-1</sup> in the spectrum of 5CuO/CeO<sub>2</sub> is compatible with the presence of crystalline CuO in this sample.<sup>50</sup> This agrees with XRD results which show that, in contrast with the results obtained for any of the Ce<sub>1-x</sub>Cu<sub>x</sub>O<sub>2</sub> catalysts, some large CuO particles are present in the 5CuO/CeO<sub>2</sub> system, thus indicating that the dispersion capacity of the ceria surface has been exceeded for this system, in agreement with previous studies.<sup>51,52</sup> The absence of crystalline CuO in the Ce<sub>1-x</sub>Cu<sub>x</sub>O<sub>2</sub> catalysts was verified as well in a previous XRD study of these catalysts employing synchrotron-derived X-rays which allowed achievement of appreciably larger S/N ratios in the diffractograms.<sup>34</sup>

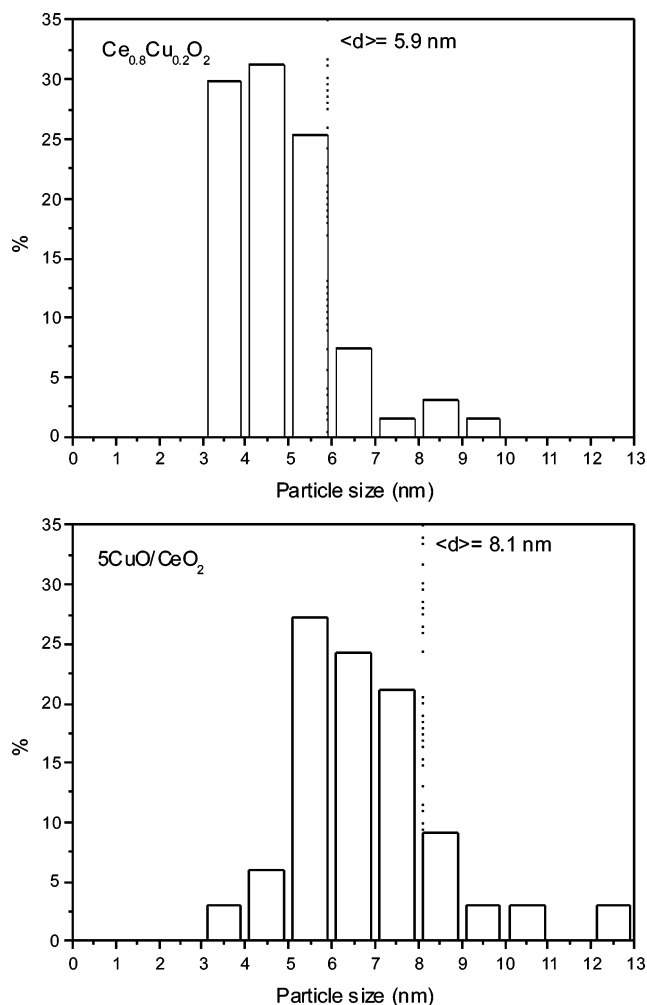


**Figure 4.** Particle size distributions of the indicated samples extracted from analysis of multiple HREM pictures. The vertical dotted line marks the average diameter ( $\langle d_{\text{pV}} \rangle = \sum n_i d_i^3 / \sum n_i d_i^2$ ) obtained from the distribution.

To complement the structural analysis, representative catalysts of the two series ( $\text{Ce}_{0.95}\text{Cu}_{0.05}\text{O}_2$ ,  $\text{Ce}_{0.8}\text{Cu}_{0.2}\text{O}_2$ ,  $1\text{CuO}/\text{CeO}_2$ , and  $5\text{CuO}/\text{CeO}_2$ ) were examined by HREM and XEDS. Many high-resolution micrographs have been recorded for  $\text{Ce}_{0.8}\text{Cu}_{0.2}\text{O}_2$  and  $5\text{CuO}/\text{CeO}_2$ . As illustrated in Figure 3, the images generally show the presence of aggregates of multiple nanoparticles displaying lattice fringes whose interplanar distances are compatible with the presence of the fluorite ceria phase in all cases. No copper-containing phase could be resolved in any of the multiple pictures taken for these samples in spite of the relatively high copper loading. This is evidence that copper must be relatively well-dispersed in all these samples. Nanocrystal particle size distributions, obtained from an analysis using Feret's diameters,<sup>53</sup> are shown in Figure 4. Volume-averaged diameters obtained from this analysis are in reasonable agreement with those estimated from XRD (Table 1).<sup>54</sup> In order to examine possible differences in the respective copper distributions, XEDS line scans across the HAADF images were acquired in different regions of every sample. During the multiple analyses performed over the four samples, it was possible to identify Ce-free zones only for the  $5\text{CuO}/\text{CeO}_2$  sample in which apparently a big (ca. 200 nm) copper oxide particle was detected (not shown), in agreement with XRD results (Figure 1). Figure 5 displays the XEDS results obtained for the four examined samples. As expected, average cerium and copper contents detected are in general agreement with the respective contents

detected by chemical analysis (see the Experimental Section). Nevertheless, appreciable differences are revealed between the two series of catalysts. A higher compositional homogeneity at a nanoscopic level appears evident for the catalysts of the  $\text{Ce}_{1-x}\text{Cu}_x\text{O}_2$  series, which suggests, in accordance with XRD (Figure 1), that copper becomes best dispersed for the samples prepared by coprecipitation within microemulsions. In turn, a decrease in the compositional homogeneity is apparently produced upon increasing the copper content of the sample in any of the series. In the case of the catalysts of the  $\text{Ce}_{1-x}\text{Cu}_x\text{O}_2$  series, this can be related to achieving saturation in the solubility capacity of copper into the ceria fluorite lattice, considering that the solubility limit is estimated (for nanosized particles) to be around  $x = 0.15$ .<sup>55</sup> In this sense, the nanoscopic XEDS analysis indicates that a perfect solid solution is not fully achieved for this type of catalyst (particularly for  $\text{Ce}_{0.8}\text{Cu}_{0.2}\text{O}_2$ ). This is probably best illustrated by the compositional line profile determined from XEDS analysis, as shown in Figure 6, in which zones enriched in either element are clearly revealed at a very local level (Figure 6a). It must be noted that fine scale fluctuations in intensity of the STEM HAADF image (Figure 6b) are correlated primarily with the sample thickness and not with the atomic composition. This is illustrated in Figure 6c in which the STEM HAADF intensity profile is compared directly with the total X-ray emission at each data point; to a good approximation the total X-ray emission will be linearly dependent on the local sample thickness.

Further insight into the structural/compositional details of these samples is provided by  $\text{Ar}^+$ -sputtering XPS experiments.<sup>18,56,57</sup> Figure 7 displays the profiles obtained during these experiments. These can be analyzed on the basis of a previously established model,<sup>56</sup> by which the profiles shown in Scheme 1 would be observed (assuming the same copper loading) depending on the occurrence of the different ideal situations depicted. According to this model and considering the relative copper contents of the samples, the profiles observed for  $\text{Ce}_{0.9}\text{Cu}_{0.1}\text{O}_2$  and  $\text{Ce}_{0.8}\text{Cu}_{0.2}\text{O}_2$  are consistent with the presence of some copper incorporated in the fluorite structure, in agreement with XRD/Raman results described above (Figures 1 and 2). This is also in accordance with observation of a small shoulder at ca. 531.5 eV in the O(1s) region of the spectrum of these samples (not shown), which is absent in the samples prepared by impregnation and which is consistent with the presence of oxygen vacancies in the samples prepared by microemulsion-coprecipitation,<sup>57,58</sup> in agreement with Raman experiments described above. Nevertheless, as inferred also from XEDS results (Figures 5 and 6), the sputtering profile observed for the two  $\text{Ce}_{1-x}\text{Cu}_x\text{O}_2$  samples does not conform to an ideal Cu–Ce mixed oxide, according to Scheme 1. In particular, the profile of  $\text{Ce}_{0.8}\text{Cu}_{0.2}\text{O}_2$  is consistent with the presence of a highly dispersed copper oxide phase at its surface, responsible of the strong maximum observed at  $t = 0$  and which can be removed by 0.5 min of sputtering (ca. 0.6 nm). Furthermore, the shoulder detected in this sample between ca. 0.5 and 3 min sputtering time suggests that such highly dispersed copper oxide particles can be deposited on a layer of copper-enriched Cu–Ce mixed oxide; i.e., the results are consistent with the presence of a gradient of copper concentration between the surface and bulk of this sample. In contrast, sample  $\text{Ce}_{0.9}\text{Cu}_{0.1}\text{O}_2$  apparently presents a higher compositional homogeneity in this sense although some small copper concentration gradient appears also evident for this sample. These results are consistent with XEDS results (Figure 5) and reveal that the saturation limit in the solubility

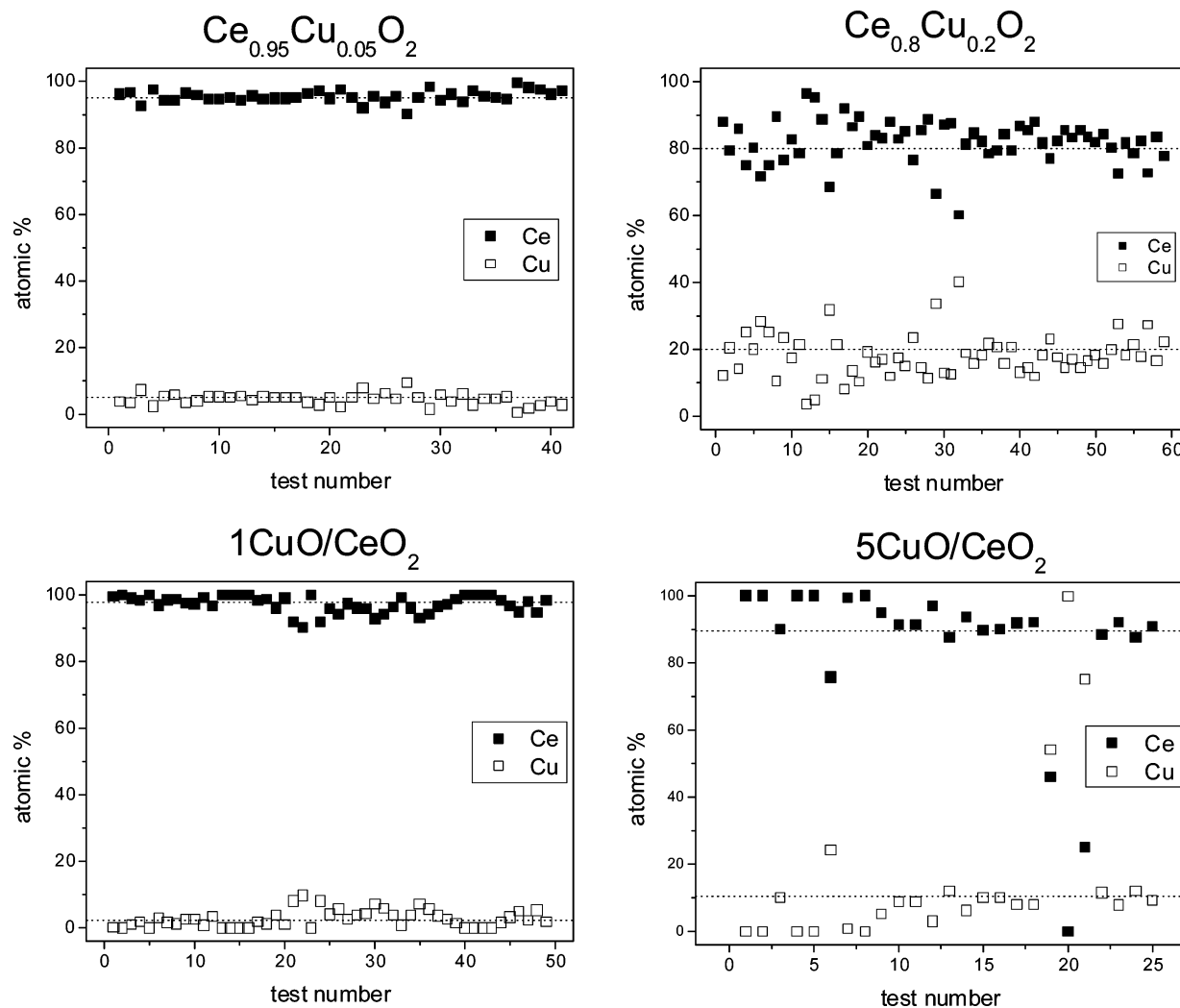


**Figure 5.** XEDS results obtained for the indicated samples. Horizontal dotted lines mark the theoretical levels of each element.

capacity of copper into the ceria nanosized particles has been exceeded for  $\text{Ce}_{0.8}\text{Cu}_{0.2}\text{O}_2$ , in agreement with the discussion above.

On the other hand, the sputtering profile observed for  $1\text{CuO}/\text{CeO}_2$  is consistent with the presence of the entire copper well-dispersed (see also details inferred from XEDS above) on the sample surface. Such a dispersed state of copper also predominates for  $5\text{CuO}/\text{CeO}_2$  although the shoulder detected in Figure 7 between ca. 0.5 and 2 min in this sample as well as the remaining high Cu/Ce ratio at >2 min are consistent with the presence of segregated big CuO particles, in accordance with XRD or TEM–XEDS experiments (Figures 1 and 5).

Electronic properties of the copper and cerium in the samples have been analyzed by XPS and XAFS. Both techniques display spectra typical of fully oxidized  $\text{Ce}^{4+}$  for all the samples (according to FA and also consistent with the ratio of the  $3d_{3/2}$  peak at ca. 916.8 eV to the total Ce 3d intensity),<sup>39,59</sup> as shown also in previous studies.<sup>34,40</sup> In the case of copper, the analysis of XPS results by means of Wagner chemical state plots (combining photoelectron and X-ray excited Auger lines)<sup>60,61</sup> indicates that copper appears also as fully oxidized  $\text{Cu}^{2+}$  in all the samples (in consistency also with the ratio observed between principal and satellite peaks in the Cu2p zone)<sup>59</sup> although the shift of Cu (2p and AES) parameters with respect to those of pure CuO indicate some modifications of its electronic properties which must be related to the size of the particles and their interaction with the support.<sup>27</sup> Wagner's chemical state plot for

the impregnated samples in Figure 8 shows that copper parameters of  $1\text{CuO}/\text{CeO}_2$  fit on the dashed line of slope  $-3$  of bulk CuO, which indicates that this is also the chemical state of the copper in this sample; however, the shift, along this line, from the bulk CuO parameters toward those found for CuO-overloaded ZSM-5 zeolites<sup>62</sup> indicates a strong interaction of thin CuO-like small clusters with the ceria.<sup>27</sup> Noteworthy, this copper is almost completely reduced to a  $\text{Cu}_2\text{O}$ -like phase after 30 min of contact with 1 torr of CO at 373 K (see the shift toward the slope  $-3$  dashed line of bulk  $\text{Cu}_2\text{O}$  in the diagram), while a complete reduction is achieved after 0.5 min of  $\text{Ar}^+$ -etching together with a deep reduction of the support (ca. 90%  $\text{Ce}^{3+}$  after 5 min). Reoxidation with 1 torr of  $\text{O}_2$  during 1 h at 473 K of the sample subjected to 10 min of sputtering restores the CuO-like chemical state of the copper remaining at the surface as well as the  $\text{Ce}^{4+}$  oxidation state of ceria. The same behavior was observed for  $5\text{CuO}/\text{CeO}_2$  though in this case the copper parameters were closer to those of the bulk CuO used as reference, which is consistent with the presence of big CuO particles poorly interacting with the ceria. These particles can be partially reduced by CO at 373 K together with the highly dispersed phase also present in this sample (see Figure 7), which gives rise to a reduced  $\text{Cu}_2\text{O}$ -like phase interacting with the reduced ceria support. The set of sputtering treatments (0.5–10 min) completely remove the more dispersed phase while it reduces to  $\text{Cu}_2\text{O}$  the big particles that remain at the surface.



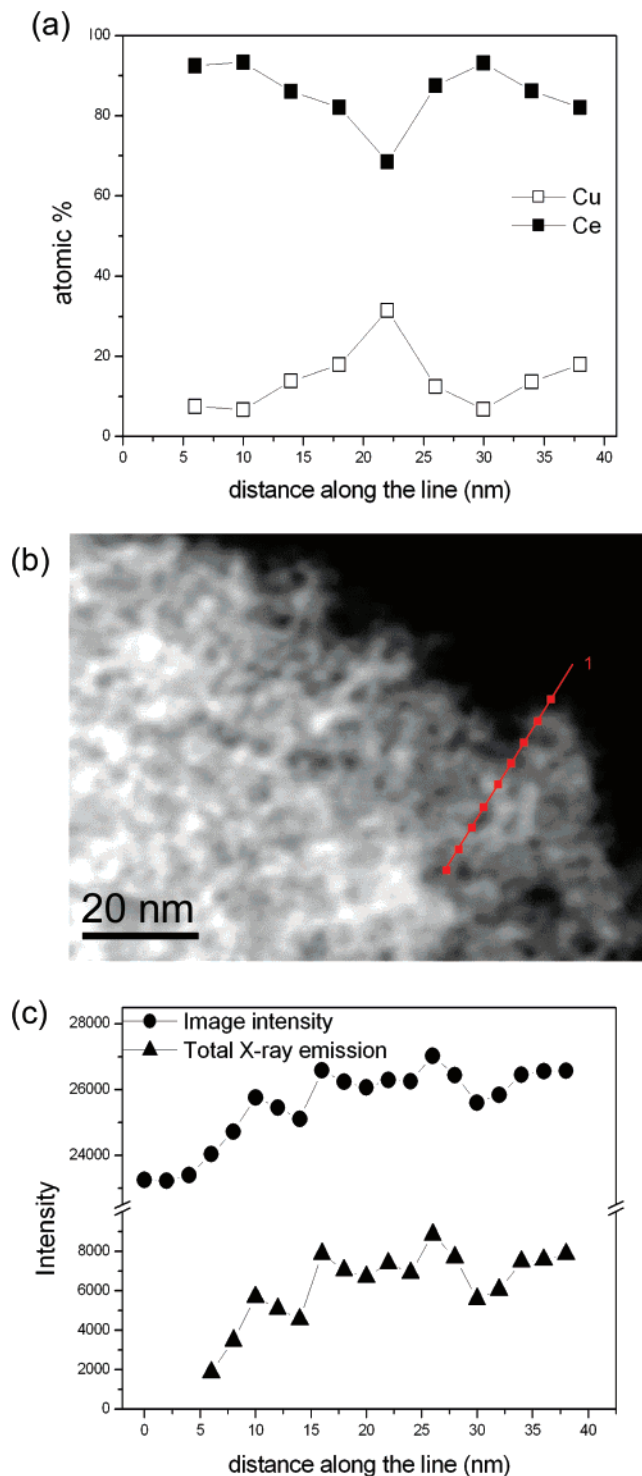


**Figure 6.** (a) Results of XEDS analysis in the points marked along the line depicted over the STEM HAADF image of  $\text{Ce}_{0.8}\text{Cu}_{0.2}\text{O}_2$  displayed in (b). (c) Comparison of the fluctuation in the intensity of the STEM HAADF image and the total X-ray emission at each data point.

Reoxidation of these particles at 473 K with 1 torr of  $\text{O}_2$  recovers their CuO-like chemical state.

Wagner's chemical state plot for  $\text{Ce}_{0.9}\text{Cu}_{0.1}\text{O}_2$  and  $\text{Ce}_{0.8}\text{Cu}_{0.2}\text{O}_2$  were rather similar between them although some small differences were apparent. Thus, the sample  $\text{Ce}_{0.8}\text{Cu}_{0.2}\text{O}_2$  was more easily reduced by CO at 373 K than  $\text{Ce}_{0.9}\text{Cu}_{0.1}\text{O}_2$ , which is consistent with the presence at its surface of a highly dispersed CuO-like phase (see Figure 7). Nevertheless, in both samples sputtering (0.5–10 min) does not lead to a complete reduction

of the copper to  $\text{Cu}^+$  probably due to the presence of subsurface unreduced copper dispersed in their bulk. This indicates a higher difficulty for the reduction of copper incorporated to the fluorite lattice, in agreement with previous investigation.<sup>34</sup> When the data for all the original samples are compared, they fit along the chemical state (slope  $-3$ ) line for CuO(bulk) but appear displaced from the CuO reference value (i.e.,  $5\text{CuO/CeO}_2 < \text{Ce}_{0.9}\text{Cu}_{0.1}\text{O}_2 < \text{Ce}_{0.8}\text{Cu}_{0.2}\text{O}_2 < 1\text{CuO/CeO}_2$ ), which indicates the same chemical state but differences in the size and/or the degree of interaction with the support of the CuO-like phase in the catalysts.

Consistent with the XPS results, X-ray absorption near-edge (XANES) spectra reveal that the chemical state of copper in the samples, while being consistent with a fully oxidized  $\text{Cu}^{2+}$  one, shows differences with that found for pure CuO.<sup>34</sup> Figure 9 displays the spectra obtained for samples of the two series in comparison with those recorded for reference compounds. The energies at which  $1s \rightarrow 4p/3d$  transitions (between ca. 8976 and 8986 eV) appear in most of the samples of the two series ( $1\text{CuO/CeO}_2$  and the three  $\text{Ce}_{1-x}\text{Cu}_x\text{O}_2$  catalysts) as well as the relatively intense peak appearing at ca. 8998 eV are indicative, upon comparison with the CuO reference, of an oxidation state of copper somewhat higher than that for the same cations in CuO. Such change must be attributed to their interaction with ceria either for the dispersed copper species at the surface or for the cations incorporated into the fluorite lattice and is consistent with previous theoretical analysis.<sup>34</sup> It may be noted that a slight downward shift of the preedge  $1s \rightarrow 3d$  peak at ca.  $8980 \text{ cm}^{-1}$  observed for  $5\text{CuO/CeO}_2$  with respect to  $1\text{CuO/CeO}_2$  (or any of the  $\text{Ce}_{1-x}\text{Cu}_x\text{O}_2$  catalysts) is observed which is again in agreement with the presence of large CuO particles in  $5\text{CuO/CeO}_2$ , in accordance also with results obtained with the other techniques.

To summarize, the characterization results obtained indicate that the bulk of the samples is constituted by nanosized particles composed by basically pure ceria in the case of the  $x\text{CuO/CeO}_2$  systems and Ce–Cu mixed oxides in the case of the  $\text{Ce}_{1-x}\text{Cu}_x\text{O}_2$  catalysts. Copper apparently appears mainly in a well (although somewhat irregularly) dispersed state on the surface of the  $x\text{CuO/CeO}_2$  systems; additionally, for the  $5\text{CuO/CeO}_2$  catalyst, a part of it segregates and forms large CuO particles. Even though copper appears comparatively more homogeneously dispersed in the catalysts of the  $\text{Ce}_{1-x}\text{Cu}_x\text{O}_2$  series, a certain copper surface segregation appears also evident in these systems, particularly when the copper loading becomes higher. In such a case, the catalyst can be probably better described as  $\text{CuO/Ce}_{1-x}\text{Cu}_x\text{O}_2$  rather than as a single solid solution of the copper. Nevertheless, the higher copper homogeneity generally achieved in the catalysts of this series suggests that the size of the copper oxide particles at their surface must be comparatively lower than that achieved for the catalysts prepared by impregnation. In this sense, recent  $\text{H}_2$ -TPR analysis revealed that the dispersed CuO species in  $\text{Ce}_{0.8}\text{Cu}_{0.2}\text{O}_2$  were more easily reducible than those in  $1\text{CuO/CeO}_2$ , which can be related to the lower size in the former although differences in the promoting effects induced by the support in each case cannot be fully discarded.<sup>63</sup> It must also be noted that achievement of a quantitative detail in the determination of the size of dispersed CuO particles by employing classical chemisorption techniques is precluded in this type of sample by the large reactivity of the support itself and (in some cases) the need of a reductive pretreatment which sinters the particles.<sup>34,64</sup> In all the calcined catalysts, copper appears in a fully oxidized  $\text{Cu}^{2+}$  chemical state with relatively small differences (except for the crystalline CuO detected in

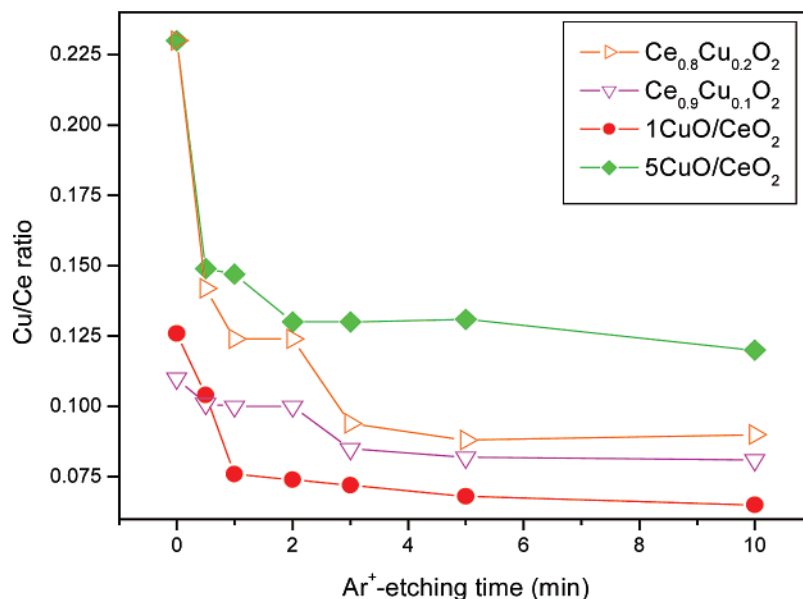
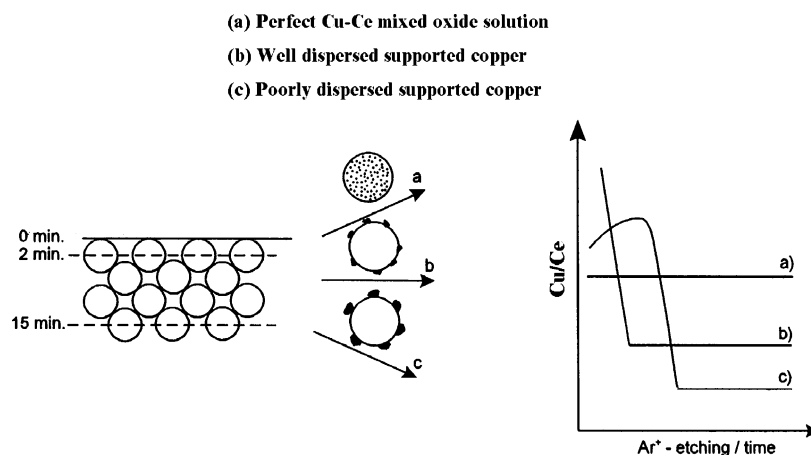


Figure 7. Evolution of the XPS detected Cu/Ce ratio as a function of the Ar<sup>+</sup>-sputtering time for the indicated samples.

#### SCHEME 1



5CuO/CeO<sub>2</sub>) between the samples concerning its electronic characteristics.

**Catalytic Properties.** Figure 10 shows the results obtained for the CO-PROX catalytic activity of the samples. As mentioned in the Experimental Section, basically CO and H<sub>2</sub> combustion are the only reactions taking place under the examined conditions. The overall evolution observed in the CO conversion profile displaying a maximum conversion at intermediate reaction temperature is (as inferred also from analysis of the CO<sub>2</sub> selectivity) a consequence of the competition between both combustion reactions, in accordance with results typically observed for this type of system.<sup>3,4,6,7,16–21</sup> Basically, as discussed in more detail elsewhere,<sup>20</sup> two regions can be generically differentiated in the activity profiles. A first one is at low temperature (<ca. 373 K, where the CO conversion increases) in which the competition between CO and H<sub>2</sub> for the active oxygen species is relatively weak.<sup>6,20</sup> A small promotion of H<sub>2</sub> oxidation by gaseous CO in this zone can explain the low-temperature minimum observed in the CO<sub>2</sub> selectivity in some cases,<sup>20</sup> Figure 10. The second region corresponds to points above the maximum CO conversion (at relatively high reaction temperature), in which CO and H<sub>2</sub> strongly compete for the available active oxygen and which results in the strong high-temperature decrease of CO<sub>2</sub> selectivity

as a consequence of the significantly higher H<sub>2</sub> partial pressure within a redox Mars–van Krevelen kinetic scheme.<sup>6,20,65</sup>

Differences are observed between the CO-PROX activity of the catalysts as a function of the copper loading and the preparation method employed. Generally speaking, the catalysts prepared by microemulsion appear more active for CO conversion although less selective than those prepared by impregnation (Figure 10). That is, considering the practical absence of side reactions (as mentioned in the Experimental Section), they are more active for both CO and H<sub>2</sub> oxidation. Nevertheless, as probably best revealed by the plot in Figure 11, the catalysts prepared by microemulsion–coprecipitation (in particular Ce<sub>0.8</sub>–Cu<sub>0.2</sub>O<sub>2</sub>) are apparently more active in relative terms for the H<sub>2</sub> oxidation reaction. On the other hand, the activity for oxidation of both CO and H<sub>2</sub> also apparently increases, for any of the two series, with increasing the copper loading. As a consequence of the balance of the different factors involved, the catalyst 1CuO/CeO<sub>2</sub> apparently results the most interesting from a practical point of view since it achieves full CO conversion at full CO<sub>2</sub> selectivity in a short temperature window of ca. 10 K. Additional experiments (not shown) have demonstrated that full CO conversion can be also attained by this catalyst in the presence of CO<sub>2</sub> and H<sub>2</sub>O in the reactant mixture (in spite of a





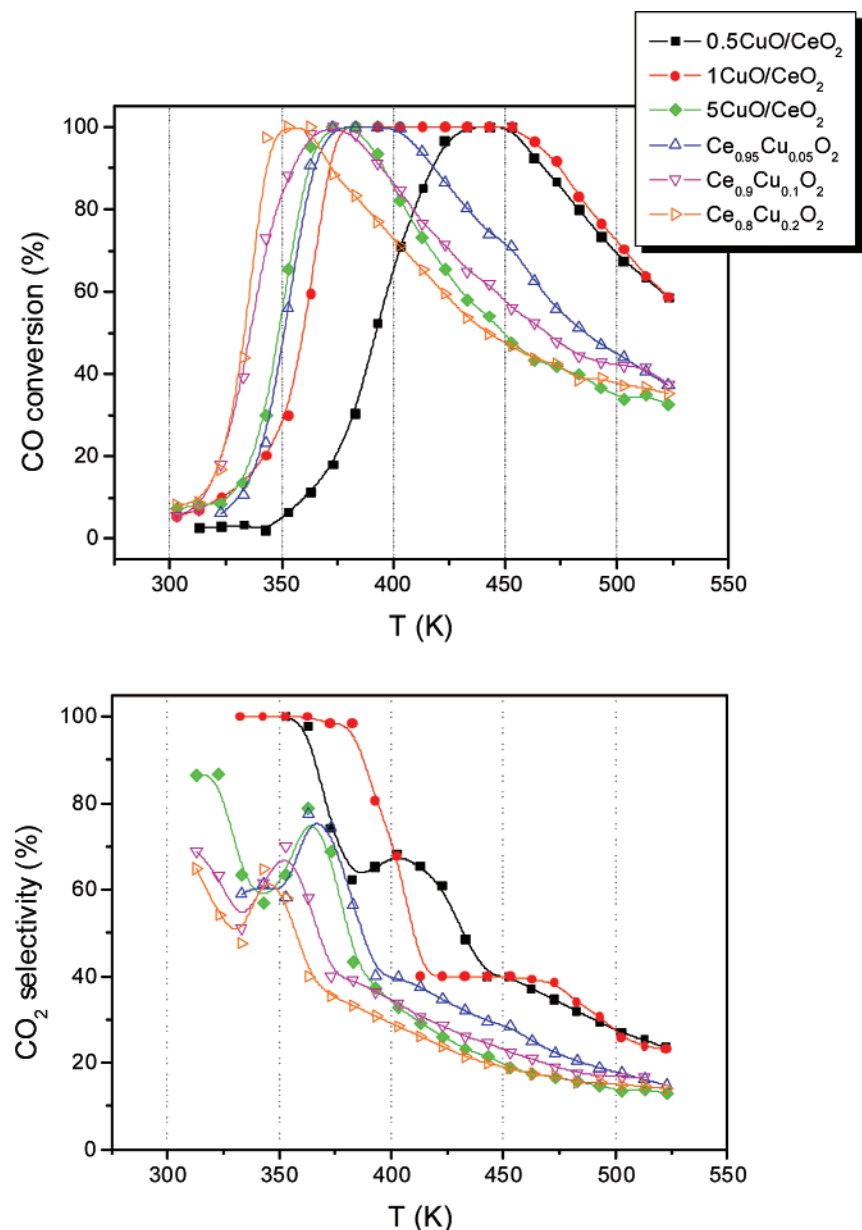


**Figure 10.** Catalytic activity under 1% CO, 1.25% O<sub>2</sub>, and 50% H<sub>2</sub> (Ar balance) for the indicated catalysts. Top: CO conversion. Bottom: selectivity to CO<sub>2</sub> among possible reactions of O<sub>2</sub> (see the Experimental Section).

species (a Cu<sup>+</sup>–carbonyl giving rise to a band at ca. 2120–2110 cm<sup>−1</sup>; assignment according to previous reports, in which details can be found).<sup>25,71</sup> The presence of these Cu<sup>+</sup>–CO species is consistent with the easy reduction of copper in the catalysts, in agreement with the XPS experiments (Figure 8).

One of the main differences between the samples is related to the intensity of this Cu<sup>+</sup>–carbonyl band. Furthermore, as displayed in Figure 13, a correlation can be established between the intensity of such carbonyl and the CO oxidation activity of the samples. Considering that formation of such carbonyl species is related to a support-promoted reduction process of the copper (taking into account that, according to XPS or XANES results—Figures 8 and 9—a fully oxidized state of copper must be present in the initial samples; consider also that the relatively low frequency of this band with respect to those expected for this type of carbonyl has been related to the interaction between these copper centers and the underlying ceria and the attribution of the adsorption center to Cu<sup>+</sup> instead of metallic copper atoms is also in agreement with their relatively high thermal stability),<sup>25,71</sup> this result clearly evidences that the active species for

CO oxidation under CO-PROX conditions are related to surface-dispersed copper oxide species interacting with the support. As detailed in previous contributions,<sup>25,27,71</sup> these copper species are easily reduced upon contact with CO at low temperature within a process in which the ceria support in contact with them can also become reduced.<sup>25,27,72</sup> Therefore, taking into account a recent model of the redox processes taking place in this type of catalyst upon interaction with CO/O<sub>2</sub>,<sup>27,73</sup> and the fact that the CO oxidation mechanism is most likely of a Mars–van Krevelen-type,<sup>6</sup> the correlation observed between the degree of copper oxide reduction and the CO oxidation catalytic activity (Figure 13) suggests that the increased extent of reduction of the copper oxide particles provide a higher amount of active sites for oxygen reduction over such particles, while the stability of the Cu<sup>+</sup> carbonyls during reaction suggests that the interfacial sites can remain essentially reduced during the process. Further experiments are in course in order to examine this hypothesis.

In principle, two basic factors can be invoked as most relevant to establish structure–activity relationships within the two series of catalysts examined in this work. The first one is related to

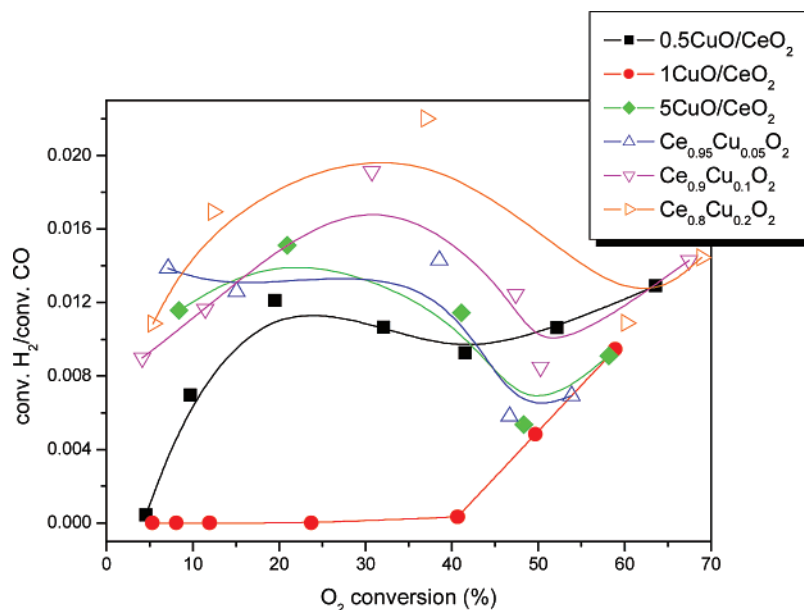


**Figure 11.** Ratio between the conversions of H<sub>2</sub> and CO with respect to the oxygen conversion obtained during the tests under CO–O<sub>2</sub>–H<sub>2</sub> (Figure 10) for the indicated catalysts.

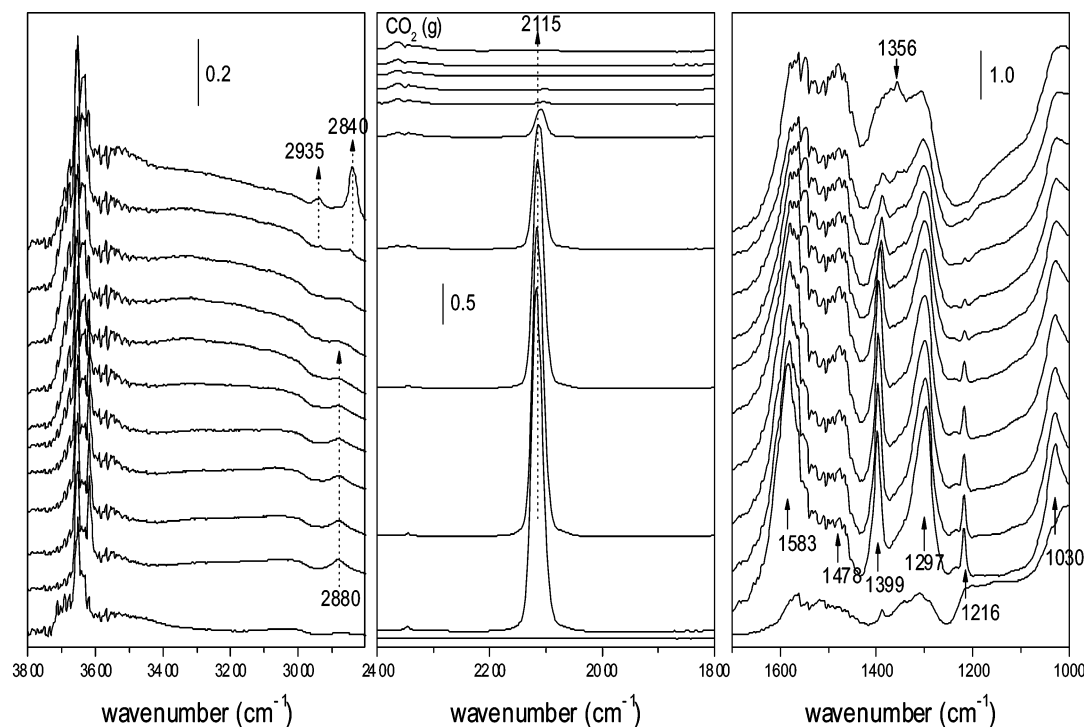


**Figure 12.** DRIFTS spectra obtained under 1% CO, 1.25% O<sub>2</sub>, and 50% H<sub>2</sub> (He balance) for 1CuO/CeO<sub>2</sub>. The spectrum at the bottom corresponds to the initial one recorded just prior to introduction of the reactant mixture. The rest correspond to spectra taken every 20 K at increasing temperature from 303 to 463 K (from bottom to top), except for the most top one which was recorded at 498 K.

the differences detected in the nature of the supports. The Cu–Ce mixed oxide present as support in the catalysts of the Ce<sub>1–x</sub>Cu<sub>x</sub>O<sub>2</sub> series could facilitate, in comparison with simple CeO<sub>2</sub> present as support in the catalysts of the *x*CuO/CeO<sub>2</sub> series, the reduction of the surface-dispersed copper oxide entities and the associated oxidation activity on the basis of decreasing the energy for oxygen vacancy formation and/or a lower activation energy for oxygen transport, as has been demonstrated to occur for other mixed oxide structures of this type.<sup>44,74</sup> A second factor can be related to differences in the respective size of the active surface-dispersed copper oxide particles. In this sense, the reduction of such particles can be favored in the catalysts of the Ce<sub>1–x</sub>Cu<sub>x</sub>O<sub>2</sub> series as a conse-

quence of their relatively lower size.<sup>44,63</sup> Alternatively, H<sub>2</sub> activation and further oxidation to water can be also favored by an enhanced copper oxide reduction and/or a more facile generation of oxygen vacancies on the support of the Ce<sub>1–x</sub>Cu<sub>x</sub>O<sub>2</sub> series catalysts. In this respect, reports are available which show that formation of oxygen vacancies defects can greatly enhance the reactivity of H<sub>2</sub>,<sup>75,76</sup> while recent H<sub>2</sub>-TPR results evidence a higher activity toward H<sub>2</sub> of Ce<sub>0.8</sub>Cu<sub>0.2</sub>O<sub>2</sub>, which is clearly the system displaying the lower CO<sub>2</sub> selectivity (Figures 10 and 11).<sup>63</sup> The achievement of relatively high levels of copper oxide dispersion has been also pointed out as detrimental to the CO<sub>2</sub> selectivity in a previous work comparing different CuO/(Ce,M)-O<sub>x</sub> (M = Zr or Tb) samples.<sup>18</sup> In definitive, it appears that the



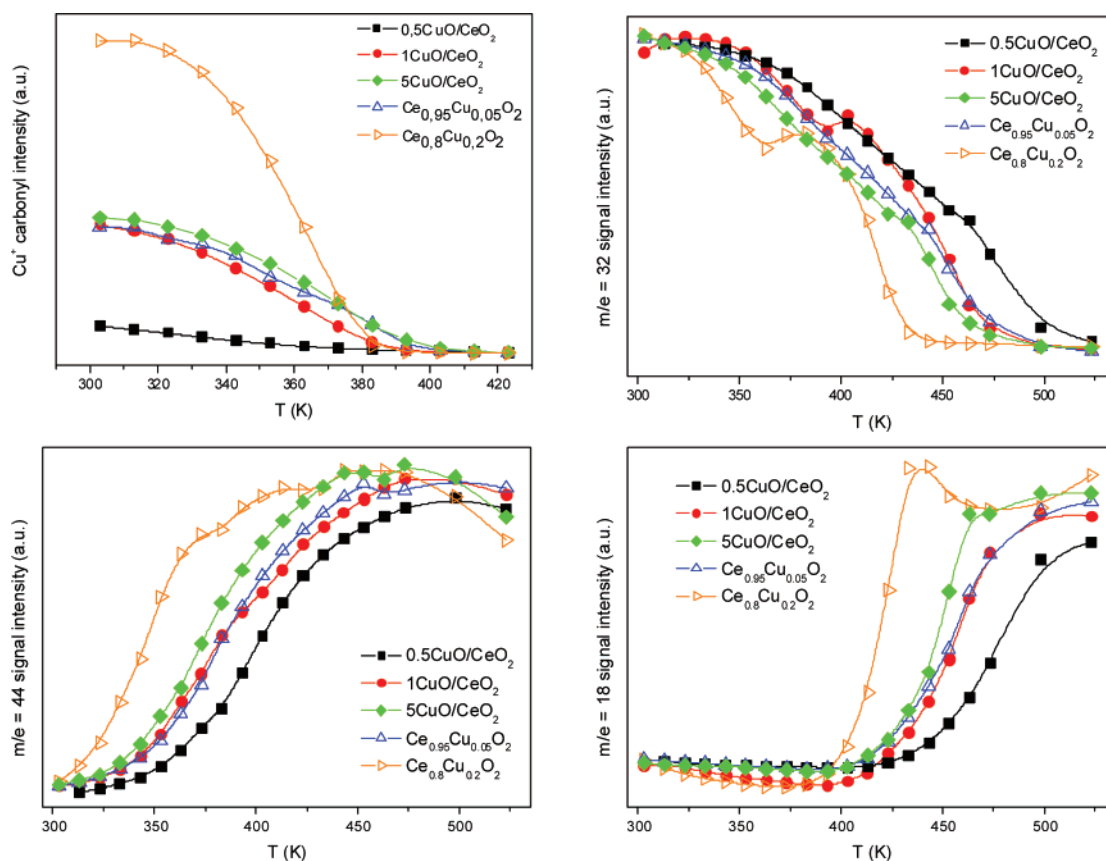


**Figure 13.** Evolution of the intensity of the  $\text{Cu}^+$ -carbonyl and of mass spectrometer signals of relevancy ( $m/e = 18, 32$ , and  $44$  essentially correspond to  $\text{H}_2\text{O}$ ,  $\text{O}_2$ , and  $\text{CO}_2$ ) to monitor the catalytic activity for the indicated samples as a function of the reaction temperature observed during the Operando-DRIFTS experiments under  $\text{CO}-\text{O}_2-\text{H}_2$ .

CO-PROX activity of this type of system can result from the balance between interrelated factors related to the presence of well-dispersed support-interacting copper oxide entities (necessary to achieve maximum CO oxidation activity) in which their reduction (and/or that of the support) could be limited to a certain level (in order to avoid a high simultaneous  $\text{H}_2$  oxidation activity).

#### 4. Conclusions

Differences between the structural characteristics of two series of nanostructured catalysts involving combinations of oxidized copper (at different loadings between ca. 2 and 20 at. %) and cerium entities and prepared by impregnation of ceria and coprecipitation within reverse microemulsions, respectively, have been evidenced. Copper appears mainly in the form of dispersed copper oxide entities at the surface of ceria, which constitutes the sample bulk, in the catalysts prepared by impregnation while a part of the copper becomes segregated as large CuO particles for the sample of highest copper loading (5 wt %) examined in this series. In contrast, copper appears at both the surface and the bulk of the samples prepared by microemulsion-coprecipitation; nevertheless, characterization at a nanoscopic level reveals that a perfect Cu–Ce oxide solid solution could not be fully achieved for these samples and surface segregation of copper oxide or copper-enriched Cu–Ce mixed oxide entities becomes more evident as the copper loading is increased. Such structural differences are reflected in some differences in the catalytic behavior for preferential oxidation of CO in a  $\text{H}_2$ -rich stream (CO-PROX). Generally speaking, samples prepared by microemulsion-coprecipitation apparently present a higher oxidation activity for both CO and

$\text{H}_2$  which generally results in catalysts which are more active but less selective for the CO-PROX process. The relatively higher copper dispersion and differences in the support nature, by which oxygen vacancies formation can be most favored in the Cu–Ce mixed oxides present in the samples prepared by microemulsion-coprecipitation, are pointed out as most relevant aspects to explain this catalytic behavior. In turn, Operando-DRIFTS experiments demonstrate that the CO oxidation activity under CO-PROX conditions is correlated to the degree of reduction achieved under reaction conditions in the surface-dispersed copper oxide entities.

**Acknowledgment.** D.G. thanks the Ministerio de Educación y Ciencia (MEC) for a FPI Ph.D. Grant under which this work was done. A.B.H. is grateful to the EU for a Marie Curie Fellowship. Thanks are due to the CICyT or MEC (Projects MAT2003-03925 and CTQ2006-15600/BQU) and Comunidad de Madrid (Project ENERCAM S-0505/ENE/000304) for financial support.

#### References and Notes

- (1) Rostrup-Nielsen, J. R.; Sehested, J.; Nørskov, J. K. *Adv. Catal.* **2002**, *47*, 65.
- (2) Fu, Q.; Saltsburg, H.; Flytzani-Stephanopoulos, M. *Science* **2003**, *301*, 935.
- (3) Avgouropoulos, G.; Ioannides, T.; Papadopolou, Ch.; Batista, J.; Hocevar, S.; Matralis, H. K. *Catal. Today* **2002**, *75*, 157.
- (4) Oh, S. H.; Sinkevitch, R. M. *J. Catal.* **1993**, *142*, 254.
- (5) Wang, J. B.; Lin, S.; Huang, T. *Appl. Catal., A* **2002**, *232*, 107.
- (6) Sedmak, G.; Hocevar, S.; Levec, J. *J. Catal.* **2003**, *213*, 135.
- (7) Kim, D. H.; Cha, J. E. *Catal. Lett.* **2003**, *86*, 107.
- (8) Korotkikh, O.; Farrauto, R. *Catal. Today* **2000**, *62*, 249.
- (9) Ghenciu, A. F. *Curr. Opin. Solid State Mater. Sci.* **2002**, *63*, 89.
- (10) Haruta, M.; Date, M. *Appl. Catal., A* **2001**, *222*, 427.

- (11) Schubert, M. M.; Venugopal, A.; Kahlich, M. J.; Plzak, V.; Behm, R. J. *J. Catal.* **2004**, *222*, 32.
- (12) Luengnaruemitchai, A.; Osuwan, S.; Gulari, E. *Int. J. Hydrogen Energy* **2004**, *29*, 429.
- (13) Deng, W.; De Jesus, J.; Saltsburg, H.; Flytzani-Stephanopoulos, M. *Appl. Catal., A* **2005**, *291*, 126.
- (14) Carrettin, S.; Concepcion, P.; Corma, A.; López Nieto, J. M.; Puentes, V. F. *Angew. Chem., Int. Ed.* **2004**, *43*, 2538.
- (15) Avgouropoulos, G.; Papavasiliou, J.; Tabakova, T.; Idakiev, V.; Ioannides, T. *Chem. Eng. J.* **2006**, *124*, 41.
- (16) Liu, Y.; Fu, Q.; Flytzani-Stephanopoulos, M. *Catal. Today* **2004**, *93–95*, 241.
- (17) Marbán, G.; Fuertes, A. B. *Appl. Catal., B* **2005**, *57*, 43.
- (18) Martínez-Arias, A.; Hungría, A. B.; Fernández-García, M.; Conesa, J. C.; Munuera, G. *J. Power Sources* **2005**, *151*, 32.
- (19) Mariño, F.; Descorme, C.; Duprez, D. *Appl. Catal., B* **2005**, *58*, 175.
- (20) Martínez-Arias, A.; Hungría, A. B.; Munuera, G.; Gamarrá, D. *Appl. Catal., B* **2006**, *65*, 207.
- (21) Park, J.-W.; Jeong, J.-H.; Yoon, W.-L.; Jung, H.; Lee, H.-T.; Lee, D.-K.; Park, Y.-K.; Rhee, Y.-W. *Appl. Catal., A* **2004**, *274*, 25.
- (22) Jobbagy, M.; Mariño, F.; Schönbrod, B.; Baronetti, G.; Laborde, M. *Chem. Mater.* **2006**, *18*, 1945.
- (23) Martínez-Arias, A.; Soria, J.; Cataluña, R.; Conesa, J. C.; Cortés Corberán, V. *Stud. Surf. Sci. Catal.* **1998**, *116*, 591.
- (24) Liu, W.; Sarofim, A. F.; Flytzani-Stephanopoulos, M. *Chem. Eng. Sci.* **1995**, *49*, 4871.
- (25) Martínez-Arias, A.; Fernández-García, M.; Gálvez, O.; Coronado, J. M.; Anderson, J. A.; Conesa, J. C.; Soria, J.; Munuera, G. *J. Catal.* **2000**, *195*, 207.
- (26) Skårman, B.; Grandjean, D.; Benfield, R. E.; Hinz, A.; Andersson, A.; Wallenberg, L. R. *J. Catal.* **2002**, *211*, 119.
- (27) Martínez-Arias, A.; Hungría, A. B.; Fernández-García, M.; Conesa, J. C.; Munuera, G. *J. Phys. Chem. B* **2004**, *108*, 17983.
- (28) Ilchev, A. N.; Firsova, A. A.; Korchak, V. N. *Kinet. Catal.* **2006**, *47*, 585.
- (29) Ratnasamy, P.; Srinivas, D.; Satyanarayana, C. V. V.; Manikandan, P.; Senthil Kumar, R. S.; Sachin, M.; Shetti, V. N. *J. Catal.* **2004**, *221*, 455.
- (30) Manzoli, M.; Di Monte, R.; Bocuzzi, F.; Coluccia, S.; Kašpar, J. *Appl. Catal., B* **2005**, *61*, 192.
- (31) Avgouropoulos, G.; Ioannides, T.; Matralis, H. *Appl. Catal., B* **2005**, *56*, 87.
- (32) Tschöpe, A.; Trudeau, M. L.; Ying, J. Y. *J. Phys. Chem. B* **1999**, *103*, 8858.
- (33) Bera, P.; Priolkar, K. R.; Sarode, P. R.; Hegde, M. S.; Emura, S.; Kumashiro, R.; Lalla, N. P. *Chem. Mater.* **2002**, *14*, 3591.
- (34) Wang, X. Q.; Rodríguez, J. A.; Hanson, J. C.; Gamarrá, D.; Martínez-Arias, A.; Fernández-García, M. *J. Phys. Chem. B* **2005**, *109*, 19595.
- (35) Shan, W.; Shen, W.; Li, C. *Chem. Mater.* **2003**, *15*, 4761.
- (36) Martínez-Arias, A.; Fernández-García, M.; Ballesteros, V.; Salamanca, L. N.; Conesa, J. C.; Otero, C.; Soria, J. *Langmuir* **1999**, *15*, 4796.
- (37) Lytle, F.; Sayers, D.; Stern, E. The History and Modern Practice of EXAFS Spectroscopy. In *Advances in X-ray Spectroscopy*; Bonnelle, C.; Mande, C., Eds.; Pergamon Press: Elmsford, NY, 1982.
- (38) Hesse, R.; Chassé, T.; Szargan, R. *Fresenius' J. Anal. Chem.* **1999**, *365*, 48.
- (39) Holgado, J. P.; Alvarez, R.; Munuera, G. *Appl. Surf. Sci.* **2000**, *161*, 301.
- (40) Wang, X. Q.; Hanson, J. C.; Rodríguez, J. A.; Gamarrá, D.; Martínez-Arias, A.; Fernández-García, M. *J. Phys. Chem. B* **2006**, *110*, 428.
- (41) Skårman, B.; Nakayama, T.; Grandjean, D.; Benfield, R. E.; Olsson, E.; Niihara, K.; Wallenberg, L. R. *Chem. Mater.* **2002**, *14*, 3686.
- (42) Zhou, X. D.; Huebner, W. *Appl. Phys. Lett.* **2001**, *79*, 3512.
- (43) Hernández-Alonso, M. D.; Hungría, A. B.; Martínez-Arias, A.; Coronado, J. M.; Conesa, J. C.; Soria, J.; Fernández-García, M. *Phys. Chem. Chem. Phys.* **2004**, *6*, 3524.
- (44) Fernández-García, M.; Martínez-Arias, A.; Hanson, J. C.; Rodríguez, J. A. *Chem. Rev.* **2004**, *104*, 4063.
- (45) Weber, W. H.; Hass, K. C.; McBride, J. R. *Phys. Rev. B* **1993**, *48*, 178.
- (46) Spanier, J. E.; Robinson, R. D.; Zhang, F.; Chan, S.-W.; Herman, I. P. *Phys. Rev. B* **2001**, *64*, 245407.
- (47) Wang, X. Q.; Hanson, J. C.; Liu, G.; Rodríguez, J. A.; Iglesias-Juez, A.; Fernández-García, M. *J. Chem. Phys.* **2004**, *121*, 5434.
- (48) McBride, J. R.; Hass, K. C.; Poindexter, B. D.; Weber, W. H. *J. Appl. Phys.* **1994**, *76*, 2435.
- (49) Nakajima, A.; Yoshihara, A.; Ishigame, M. *Phys. Rev. B* **1994**, *50*, 13297.
- (50) Xu, J. F.; Ji, W.; Shen, Z. X.; Li, W. S.; Tang, S. H.; Ye, X. R.; Jia, D. Z.; Xin, X. Q. *J. Raman Spectrosc.* **1994**, *30*, 413.
- (51) Tang, X.; Zhang, B.; Li, Y.; Xu, Y.; Xin, Q.; Shen, W. *Catal. Today* **2004**, *93–95*, 191.
- (52) Chen, H.; Zhu, H.; Wu, Y.; Gao, F.; Dong, L.; Zhu, J. *J. Mol. Catal.* **2006**, *255*, 254.
- (53) Matyi, R. J.; Schwartz, L. H.; Butt, J. B. *Catal. Rev.—Sci. Eng.* **1987**, *29*, 41.
- (54) Adams, C. R.; Benesi, H. A.; Curtis, R. H.; Meisenheimer, R. G. *J. Catal.* **1962**, *1*, 336.
- (55) Knauth, P.; Schwitzgebel, G.; Tschöpe, A.; Villain, S. *J. Solid State Chem.* **1998**, *140*, 295.
- (56) González-Elipe, A. R.; Holgado, J. P.; Alvarez, R.; Espinós, J. P.; Fernández, A.; Munuera, G. *J. Catal.* **1991**, *130*, 627.
- (57) Martínez-Arias, A.; Fernández-García, M.; Hungría, A. B.; Conesa, J. C.; Munuera, G. *J. Phys. Chem. B* **2003**, *107*, 2667.
- (58) Holgado, J. P.; Munuera, G.; Espinós, J. P.; González-Elipe, A. R. *Appl. Surf. Sci.* **2000**, *158*, 164.
- (59) Skarman, B.; Grandjean, D.; Benfield, R. E.; Hinz, A.; Andersson, A.; Wallenberg, L. R. *J. Catal.* **2002**, *211*, 119.
- (60) Wagner, C. D. *Faraday Discuss. Chem. Soc.* **1975**, *60*, 291.
- (61) Moretti, G. *J. Electron Spectrosc. Relat. Phenom.* **1998**, *95*, 95.
- (62) Grünert, W.; Hayes, N. W.; Joyner, R. W.; Shpiro, E. S. *J. Phys. Chem.* **1994**, *98*, 10832.
- (63) Gamarrá, D.; Hornés, A.; Koppány, Zs.; Schay, Z.; Munuera, G.; Soria, J.; Martínez-Arias, A. *J. Power Sources* **2007**, *169*, 110.
- (64) Bernal, S.; Calvino, J. J.; Gatica, J. M.; López Cartes, C.; Pintado, J. M. In *Catalysis by Ceria and Related Materials*; Trovarelli, A., Ed.; Imperial College Press: London, 2002; p 85.
- (65) Mars, P.; van Krevelen, D. W. *Chem. Eng. Sci.* **1954**, *3* (special supplement), 41.
- (66) Badri, A.; Binet, C.; Lavalley, J.-C. *J. Chem. Soc., Faraday Trans.* **1996**, *92*, 4669.
- (67) Binet, C.; Daturi, M.; Lavalley, J.-C. *Catal. Today* **1999**, *50*, 207.
- (68) Li, C.; Sakata, Y.; Arai, T.; Domen, K.; Maruya, K.-I.; Onishi, T. *J. Chem. Soc., Faraday Trans. 1* **1989**, *85*, 929.
- (69) Li, C.; Sakata, Y.; Arai, T.; Domen, K.; Maruya, K.-I.; Onishi, T. *J. Chem. Soc., Faraday Trans. 1* **1989**, *85*, 1451.
- (70) Pozdnyakova, O.; Teschner, D.; Woosch, A.; Kröhnert, J.; Steinhauer, B.; Sauer, H.; Toth, L.; Jentoft, F. C.; Knop-Gericke, A.; Paál, Z.; Schlögl, R. *J. Catal.* **2006**, *237*, 1.
- (71) Martínez-Arias, A.; Fernández-García, M.; Soria, J.; Conesa, J. C. *J. Catal.* **1999**, *182*, 367.
- (72) Martínez-Arias, A.; Fernández-García, M.; Hungría, A. B.; Iglesias-Juez, A.; Gálvez, O.; Anderson, J. A.; Conesa, J. C.; Soria, J.; Munuera, G. *J. Catal.* **2003**, *214*, 261.
- (73) Martínez-Arias, A.; Gamarrá, D.; Fernández-García, M.; Wang, X. Q.; Hanson, J. C.; Rodríguez, J. A. *J. Catal.* **2006**, *240*, 1.
- (74) Esch, F.; Fabris, S.; Zhou, L.; Montini, T.; Africh, C.; Fornasiero, P.; Comelli, G.; Rosei, R. *Science* **2005**, *309*, 752.
- (75) Lamonier, C.; Ponchel, A.; D'Huysser, A.; Jalowiecki-Duhamel, L. *Catal. Today* **1999**, *50*, 247.
- (76) Kim, J. Y.; Rodríguez, J. A.; Hanson, J. C.; Frenkel, A. I.; Lee, P. L. *J. Am. Chem. Soc.* **2003**, *125*, 10684.